Journal of Materials Chemistry A

Accepted Manuscript

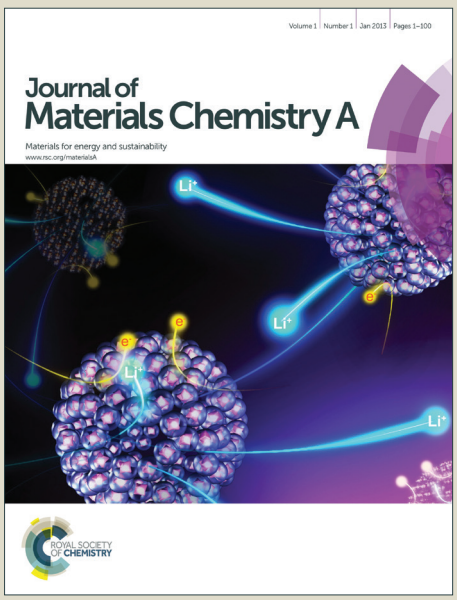

ROYAL SOCIETY OF CHEMISTRY

www.rsc.org/materialsA

Cite this: DOI: 10.1039/c0xx00000x

www.rsc.org/xxxxxx

ARTICLE TYPE

Size-Selective Synthesis of Mesoporous $LiFePO_4$/C Microspheres based on Nucleation and Growth Rate Control of Primary Particles

Min-Young Cho,[a,b] Haegyeom Kim,[c] Hyungsub Kim,[c] Young Su Lim,[a] Kwang-Bum Kim,[b] Jae-Won Lee,[d] Kisuk Kang[c,e]* and Kwang Chul Roh[a,]*

Received (in XXX, XXX) Xth XXXXXXXXX 20XX, Accepted Xth XXXXXXXXX 20XX
DOI: 10.1039/b000000x

Because of the on-going miniaturization of devices powered by lithium-ion batteries, the realization of a high tap density that sustains a high power output is crucial to enhancing the low intrinsic volumetric energy density of $LiFePO_4$ (LFP), one of the most extensively studied cathode materials. To increase the tap density of LFP, we report a synthetic method that allows microscale size control of a $LiFePO_4$ precursor with a mesoporous structure based on changes in chemical potential and nucleation and growth rates by surfactant addition. The carbon-coated $LiFePO_4$ particles prepared from the precursors had diameters and tap densities in the range of 3–7 μm and 1.3–1.5 g cm^{-3}, respectively, depending on the surfactant concentration. The particles exhibited negligible antisite defects (approximately 2%), and showed a high volumetric capacity of approximately 190 mAh cm^{-3} at 0.1 C-rate and an excellent rate performance of 80 mA h g^{-1} at 30 C-rate.

Introduction

Lithium iron phosphate ($LiFePO_4$, LFP) is an attractive cathode material for Li-ion batteries (LIBs) because it provides a high theoretical capacity (170 mAh g^{-1}), superior cycle life, and thermal stability.[1] However, the material has an intrinsically low electronic conductivity (approximately 10^{-9}–10^{-10} S cm^{-1}) owing to discontinuous domains in the corner-shared FeO_6 network in the crystal structure. It also exhibits slow ion diffusion kinetics owing to the blocking of one-dimensional channels by defects and impurities.[2–4]

Numerous methods have been developed to enhance the rate capability of LFP, such as application of conductive carbon coatings and methods providing reduced particle sizes.[5] The former can improve the electronic conductivity, suppress particle growth during calcination, and lower the susceptibility of Fe ions to oxidation. Over the years, carbon coatings have been applied by high-temperature pyrolysis of organic precursors such as sucrose,[6,7] citric acid,[8] pitch carbon,[9] and polypyrrole.[10] Meanwhile, the latter methods improve the ionic diffusivity by increasing the number of active sites at the electrolyte/LFP interface and shortening the Li ion transport path lengths along one-dimensional [010] channels.[3,11] Thus, nanosized LFP can improve the rate performance. However, nanosized LFP requires a higher amount of binder material because of the high surface-to-volume ratio of the nanosized materials. This can significantly decrease the volumetric energy density of the electrode. The ongoing miniaturization of electronic devices and the use of LIBs in large-scale industrial applications such as hybrid electric vehicles require that the active materials for LIBs have not only the aforementioned properties of nanosized materials, but also high tap densities, which are related to the particle size and the porous structure that facilitates percolation of the electrolyte.

To increase the tap density while maintaining the merits of nanosized materials, LFP microspheres with interconnected open pores would be useful because they combine high volumetric energy densities with increased numbers of effective active sites. Hence, many researchers have recently reported carbon-coated LFP (LFP/C) microspheres with high tap densities produced using coprecipitation,[9] hydrothermal,[12] and solvothermal methods.[13] For example, Oh *et al*. synthesized 8 μm carbon-coated LFP (LFP/C) spheres with a tap density of 1.5 g cm^{-3} by controlling the pH during coprecipitation. These spheres demonstrated a specific capacity of 80 mA h g^{-1} at 20 C-rate.[9] Similarly, Qian *et al*. synthesized 3 μm LFP/C spheres with a tap density of 1.4 g cm^{-3} by hydrothermal synthesis using sucrose as an additive; these spheres exhibited a specific capacity of 71 mA h g^{-1} at 30 C-rate.[12] We have also recently reported mesoporous LFP/C spheres, 1.5–2 μm in diameter, produced using a solvothermal process; these exhibited a specific capacity of 86 mA h g^{-1} at 20 C-rate.[13]

Herein, we report a facile method to adjust the size of microscale LFP spheres using cetyltrimethylammonium bromide (CTAB) as a surfactant, and we discuss the mechanism of the formation of differently sized microsphere precursors in terms of tuning the nucleation and growth rates of primary particles. Moreover, the electrochemical properties of LFP spheres of different sizes are investigated.

Experimental

Preparation of precursors and $LiFePO_4$/C

CTAB was dissolved in absolute ethanol (40 mL) at room

temperature, and $CH_3COOLi{\cdot}2H_2O$, $Fe(NO_3)_3{\cdot}9H_2O$, and H_3PO_4 (85 wt%) were successively added in a molar ratio of Li/Fe/P = 1:1:1. The solution was stirred for 0.5 h and transferred to a 100 mL Teflon-lined autoclave. The autoclave was sealed and incubated at 160°C for 3 h. After cooling to room temperature, the LFP precursor was collected by filtration and washed with distilled water to remove excess CTAB. The precursor was dried at 80°C for 24 h in air. To remove any remaining Br ions, the precursor was preheated at 500°C for 6 h (heating and cooling rates: 2°C min^{-1}) in a hydrogen/argon mixture (5 vol% H_2). The preheated LFP was carbon-coated by impregnating the precursor with citric acid (citric acid/preheated LFP = 1:2.5 wt% in absolute ethanol). The mixture was stirred at 90°C until the ethanol had evaporated. The solid mixture was then heated at 700°C for 12 h in a hydrogen/argon mixture (5 vol% H_2). Using the above process, the as-prepared precursors designated C1-LFP, C2-LFP, and C3-LFP were prepared using CTAB concentrations of 2.75, 5.49, and 8.23 mmol, respectively. The carbon-coated $LiFePO_4$, samples are designated C1-LFP/C, C2-LFP/C, and C3-LFP/C.

Characterization

The morphologies and particle size distributions of the synthesized samples were investigated using field-emission scanning electron microscopy (FE-SEM, JEOL JSM-6700F). The crystalline phases and lattice parameters of the samples were analyzed by measuring their X-ray diffraction (XRD) patterns (Rigaku D/Max-2500/PC) at 0.02 steps/4 s using Cu Kα radiation (λ = 1.54 Å) over a 2θ range of 10–100°. The XRD data were refined using the Rietveld method with FullProf software. FT-IR (JASCO FT/IR 4200) was conducted using KBr pellets. To analyze the chemical states of the synthesized samples, X-ray photoelectron spectroscopy (XPS) was performed with a PHI 5000 VersaProbe spectrometer using Al Kα radiation ($h\upsilon$ = 1486.6 eV). The carbon contents of the LFP/C particles were determined using a Carbon/Sulfur determinator (LECO Corp., CS600). The specific surface areas and pore distributions were measured by Brunauer-Emmett-Teller analysis (BELSORP-miniII, BEL Japan, Inc.). To further confirm the materials' porosities, cross-sections were imaged by focused ion beam (FIB) analysis (FEI Helios NanoLab™ 600). To measure the tap density, 2 g of the product was placed in a small measuring cylinder and repeatedly tapped (1000 times) using a tap density tester (Logan Instruments, TAP-2S).

Electrochemical measurements

Electrodes were prepared by coating a slurry containing the active LFP material, Super-P carbon black conductive additive (MMM, Belgium), and a polyvinylidene fluoride binder (Kurea, Japan) at a weight ratio of 80:15:5 onto an aluminum-foil current collector. The thickness of the electrode was controlled to approximately 50 μm (including the 20 μm Al foil) by roll-pressing, and the electrode densities were calculated as approximately 1.18, 1.25, and 1.3 g cm^{-3} for C1-LFP/C, C2-LFP/C, and C3-LFP/C, respectively. Lithium metal was used as the counter electrode. The electrochemical properties of the samples were examined using a coin cell (CR 2016) that was assembled in an argon-filled glove box. Microporous polyethylene and a 1.0 M $LiPF_6$ solution in ethylene carbonate/ethyl methyl carbonate (1:2 vol%; Cheil Industries, Korea) were used as the separator and electrolyte, respectively. Galvanostatic charge and discharge tests were carried out at room temperature at working voltages of 2.0 to 4.5 V vs. Li^+/Li.

Results and discussion

The morphologies and particle sizes of the as-synthesized LFP precursors were confirmed by FE-SEM (Fig. 1). All precursors have uniform size distributions and microsphere morphologies, but the average particle sizes (3–7 μm) are strongly influenced by the CTAB concentration. Typically, CTAB suppresses the crystal growth of materials; it has been used previously in the hydrothermal process to prepare nanosized LFP.[14] These LFP particles had sizes of 50 and 90–100 nm for CTAB concentrations of 13.7 and 4.11 mmol, respectively. In our synthesis, the primary particle sizes consisting of microsphere precursors increased proportionally with the CTAB concentration (Fig. 1(a), (b) and (c), insets). To confirm the mechanism of primary particle formation, intermediate particles were collected at different reaction times; FE-SEM images are shown in Fig. S1†.

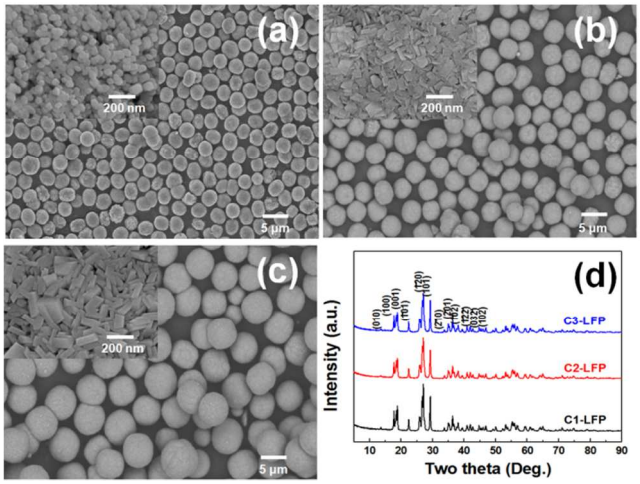

Fig. 1 FE-SEM images of as-synthesized precursors for different CTAB concentrations: (a) C1-LFP, (b) C2-LFP, and (c) C3-LFP; (d) XRD patterns. Insets are magnified images on the surface of single particle.

The overall mechanisms of precursor formation are shown in Scheme 1. The process can be classified into three steps, the first of which is nucleation and growth (initial reaction, ~1 h). In this phase, particle sizes increase from 20 to 90 nm with increasing concentrations of CTAB after ~0.5 h. In our system, CTAB micellization does not occur because the critical micelle concentration (CMC = 0.24 mol L^{-1}) of CTAB is higher in ethanol than in water (CMC = 0.9 mmol L^{-1}).[15] Also, CTAB can react with H_3PO_4 polyanions as a cationic polymer; the dissolved CTAB ionizes to form CTA^+, which has a positively charged tetrahedral head group and a long hydrophobic alkyl tail, and H_3PO_4 becomes negatively charged. Electrostatic interactions then cause the released PO_4^{3-} ions to be surrounded by CTA^+ ions, while the hydrophobic tails limit the interactions of Li^+ and Fe^{3+} ions with PO_4^{3-}.[16]

Thus, the nucleation rate for the molecular precursor is reduced due to limited chemical reaction in proportion to the concentration of CTAB. The correlation between the nucleation

rate and surfactant concentration can be expressed as follows:[17,18]

$$J_N = B_N \exp(-\Delta G^N/RT) \quad (1)$$

$$\Delta G^N = 16\,\pi\gamma^3 V_m^2/3|\Delta\mu|^2 \quad (2)$$

$$\Delta\mu = RT\ln S \quad (3)$$

$$S = C/C_s \quad (4)$$

where, J_N (the crystal nucleation rate per unit volume) is determined by ΔG^N (the activation energy of homogeneous nucleation), which in turn depends on $\Delta\mu$ (the chemical potential difference). Because the increase of C_s (equilibrium saturation) by the molecular precursor forms stable complexes, the addition of a surfactant during nucleation induces a decrease in S (the degree of supersaturation), which then leads to a decrease in $\Delta\mu$ and a concomitant increase in ΔG^N. Therefore, the nucleation rate (J_N) decreases and relatively large nuclei accrue. As a consequence, larger amorphous particles are formed with increasing CTAB concentration. The other terms in the equations are defined as: B_N, a pre-exponential factor; γ, the surface energy of the particle; V_m, the molar volume of the solid; and C, the solute concentration.

The second stage (at 1–1.5 h) involves dissolution and crystallization. In this step, unstable amorphous particles gradually dissolve due to the increase of solubility by acidity (precursor solution pH ≈ 1) and high temperature; then the particles crystallize through Ostwald ripening.[19] During this phase, the primary particle morphologies are transformed to plate-like, and their sizes increase to 50–150 nm with the increase of CTAB concentration.

In the last step, self-assembly (1.5–3 h), the primary particles continuously self-assemble into microspheres, driven by the reduction in the surface free energy,[12] and primary particles consisting of microspheres grow larger during the long reaction time.

Thus, the sizes of microsphere LFP precursors can be adjusted through control of the primary particle size, and the nucleation and growth rates can be changed by the CTAB concentration.

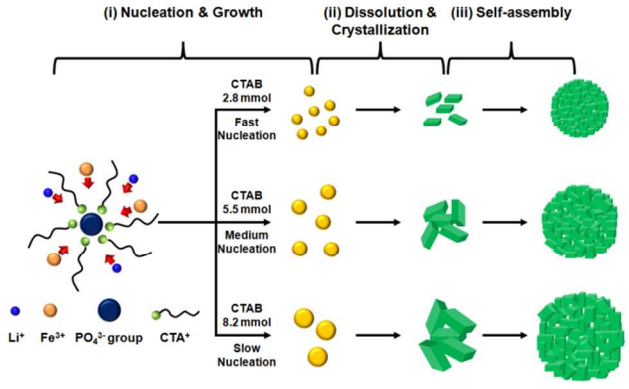

Scheme 1. Mechanisms of precursor formation

The XRD patterns of the as-synthesized precursors for different CTAB concentrations are shown in Fig. 1(d). The precursors were confirmed to be highly crystalline, and all peaks were well indexed to the triclinic structure of $LiFe(PO_4)(OH)$.

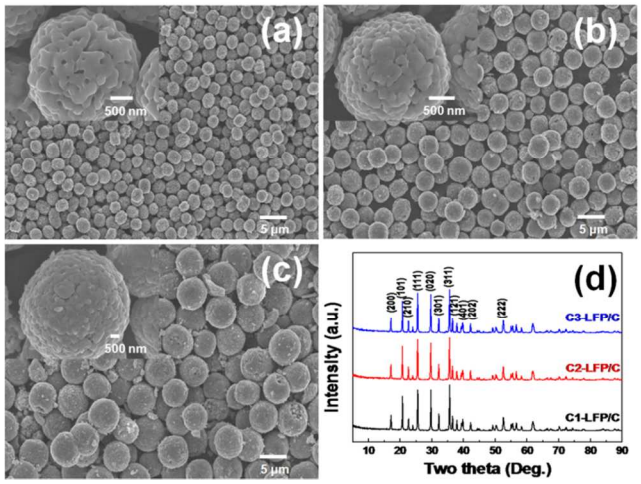

Fig. 2 FE-SEM images of carbon-coated LFPs for different CTAB concentrations: (a) C1-LFP/C, (b) C2-LFP/C, and (c) C3-LFP/C. (d) XRD patterns of the LFP/C samples. Insets are magnified images of single particle.

Figure 2(a), (b) and (c) shows FE-SEM images of LFP/Cs prepared by heat treatment of the precursors after impregnation with citric acid. The precursors and LFP/C particles have similar sizes and morphologies; the samples exhibit the orthorhombic olivine structure (*Pnma*) without impurity phases. The mean crystallite size for each LFP/C sample was calculated using Scherrer's equation, *i.e.*, $d = 0.9\,\lambda/\beta_{1/2}\cos\theta$, where λ is the wavelength and $\beta_{1/2}$ is the peak width at half height of the (101), (111), (020), and (311) peaks. The calculated unit cell volumes are 290.04, 290.21, and 290.12 Å^3 for C1-LFP/C, C2-LFP/C, and C3-LFP/C, respectively. Lattice parameters are reported in Table S1†.

The pore distributions of the precursors and LFP/C particles were determined from nitrogen adsorption-desorption measurements (Fig. S2†). All samples show type-IV isotherms with large type H2 hysteresis loops, indicative of a mesoporous structure. The specific surface areas and mean pore sizes of the precursors and LFP/C particles are shown in Table. 1.

The mesoporous structures of the interiors of the LFP/C particles were also demonstrated by the cross-sectional images of the samples obtained using FIB analysis (Fig. 3(a), (b) and (c)). Significantly, interconnected mesoporous structures were observed. These results indicate that an improvement in the rate performance could be expected by the increased effective reaction area and facile penetration of the electrolyte.

Table 1 Specific surface areas and mean pore sizes for the precursors and LFP/C particles

Sample	C1-LFP	C2-LFP	C3-LFP
Surface area ($m^2\ g^{-1}$)	9.4	12.9	9.8
Mean pore diameter (nm)	15.9	15.3	16.6
Sample	C1-LFP/C	C2-LFP/C	C3-LFP/C
Surface area ($m^2\ g^{-1}$)	7.3	9.4	8.5
Mean pore diameter (nm)	6.0	6.0	6.8

Antisite defects, $Fe^{\bullet}_{Li}$ (Fe^{2+} on Li^{+} sites), are related to the degree of Li ion migration, which directly affects the electrochemical performance. The LFP particles formed by the hydrothermal process have antisite defects due to changes in the force constant between the P and O atoms in the PO_4 tetrahedron at the low reaction temperature.[3,20]

To investigate the concentrations of antisite defects, we carried out Rietveld refinements of the XRD patterns (Fig. S3†). Antisite defects constituted approximately 2% of all samples, less than half that observed for hydrothermally prepared LFP (4.6%).[21]

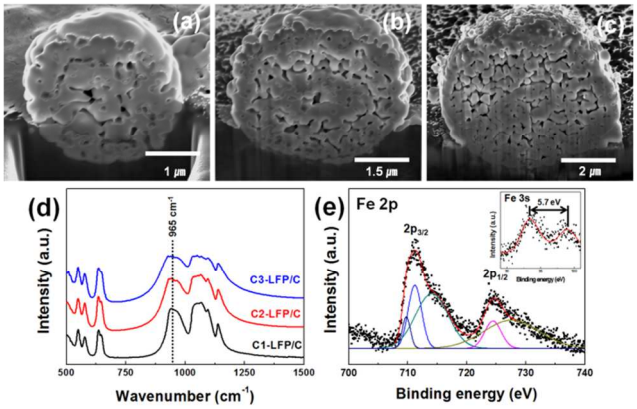

Fig. 3 Cross-sectional images of (a) C1-LFP/C, (b) C2-LFP/C, and (c) C3-LFP/C obtained by FIB analysis. (d) FT-IR spectra. (e) Fe 2*p* XPS spectra featuring Fe $2p_{3/2}$ and Fe $2p_{1/2}$ peaks for C3-LFP/C (inset shows the Fe 3*s* spectrum, with a splitting of 5.7 eV).

To confirm these results, we further analyzed the stretching vibration of the PO_4 tetrahedron using FT-IR spectroscopy. Typically, the symmetric P–O stretching vibration of hydrothermally prepared LFP is located at 1000 cm^{-1}, but it appears red-shifted to approximately 965 cm^{-1} in Fig. 3(d). This is consistent with the results for solvothermally synthesized LFP in reaction media of low dielectric constants such as ethylene glycol and ethanol, and proves that the concentration of antisite defects is decreased.[3]

To investigate the valence state of the Fe ions when Fe^{3+} is used as the raw material, we examined the chemical states of the LFP/Cs by XPS (Fig. 3(e)). Here, only the results for C3-LFP/C are shown, since the XPS spectra of C1-LFP/C and C2-LFP/C were identical. The Fe 2*p* spectrum consists of two parts, Fe $2p_{3/2}$ and Fe $2p_{1/2}$, because of spin-orbit coupling of the partially filled *d*-orbitals (characteristic of transition metal ions). The Fe $2p_{3/2}$ and Fe $2p_{1/2}$ spectra are each divided into peaks at 709.7 and 711.2 eV, and "shake-up" satellite peaks at 724.4 and 727.6 eV, respectively. The peaks corresponding to Fe 3*s* are located at 93.3 eV and 99.0 eV, indicating a binding energy splitting of ΔE = 5.7 eV (*i.e.*, ΔE of Fe^{3+} = ~6.5 eV).[22] Thus, Fe^{3+} was completely reduced to Fe^{2+}, since all Fe 2*p* and Fe 3*s* peaks correspond to Fe^{2+}.

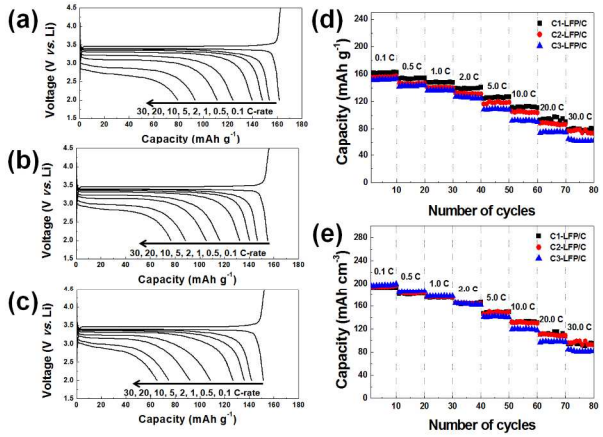

Fig. 4 Discharge curves for (a) C1-LFP/C, (b) C2-LFP/C, and (c) C3-LFP/C. A constant current of 0.1 C-rate was used for each charging step, while the discharge current varied from 0.1 to 30 C-rate. (d) Gravimetric capacity and (e) volumetric capacity at different current rates.

The carbon contents of the particles were measured using a Carbon/Sulfur determinator. To estimate the carbon content originating from CTAB, we first analyzed the LFP precursors, which exhibited carbon contents below 0.1 wt% for all samples. This suggested that CTAB-derived carbon was absent and that any carbon present would result from the addition of citric acid. Analysis of the carbon-coated material (after citric acid treatment) indicated a value of approximately 3 wt%, as listed in Table S2†. Thus, CTAB-derived carbon is absent, and the carbon results only from the addition of citric acid. The highly uniform coatings with low carbon contents and the controlled microscale size of the particles consequently give rise to high tap densities of approximately 1.3, 1.4, and 1.5 g cm^{-3} for C1-LFP/C, C2-LFP/C, and C3-LFP/C, respectively.

Figure 4(a), (b), and (c) shows the discharge curves for C1-LFP/C, C2-LFP/C, and C3-LFP/C at different rates. A constant current of 0.1 C-rate (17 mA g^{-1}) was used for each charging step, while discharging was performed at progressively increasing rates. Each sample displays discharge voltage plateaus at approximately 3.4 V. At 0.1 C-rate, the discharge capacities of C1-LFP/C, C2-LFP/C, and C3-LFP/C are 161, 155, and 151 mA h g^{-1}, respectively, indicating that over 90% of the theoretical capacity (170 mA h g^{-1}) can be attained for all samples. For C1-LFP/C, a relatively high capacity value of 80 mA h g^{-1} was measured even at 30 C-rate (5100 mA g^{-1}).

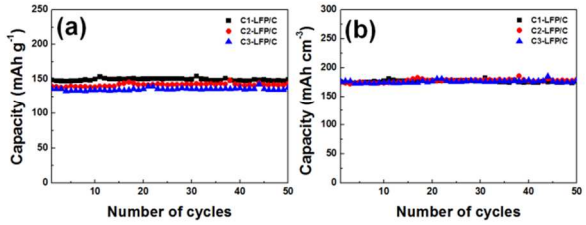

Fig. 5 Cycling performance in terms of (a) gravimetric and (b) volumetric capacity at charge/discharge currents of 1 C-rate. The gravimetric capacities are approximately 150, 140, and 135 mA h g^{-1}, and the volumetric capacities are approximately 176, 175, and 176 mA h cm^{-3} for C1-LFP/C, C2-LFP/C, and C3-LFP/C, respectively. The retention ratios of all samples approach 100%.

In order to compare the effects of tap density, the rate performances as measured using the gravimetric and volumetric capacities are shown in Fig. 4(d) and (e). The volumetric discharge capacities at 0.1 C-rate of C1-LFP/C, C2-LFP/C, and C3-LFP/C are 191, 194, and 197 mA h cm^{-3}, respectively. These high values are attributed to the aforementioned high tap densities of the LFP particles. Furthermore, the observed capacities at 1 C-rate (170 mA g^{-1}) are very stable with negligible decay (~100% capacity retention) for all samples under cycling (Fig. 5).

The excellent rate and cycling performance of the LFP/Cs for various particle sizes may result from their inherent mesoporous structures, as well as the good electronic conductivity of the carbon coating and the diminished contribution of antisite defects.

Conclusions

In summary, CTAB plays an essential role in adjusting the morphology and size of the primary LFP particles by controlling the nucleation and growth rates during synthesis. With this surfactant, LFP microspheres of various sizes can be obtained. The solvothermal synthesis of LFP particles using CTAB and ethanol has the following advantages: (i) generation of micron-sized mesoporous spherical particles, (ii) straightforward control of the particle size and thus the tap density by adjusting the CTAB concentration, (iii) formation of crystal structures without significant impurities, and (iv) a reduced concentration of the $Fe^{\bullet}_{Li}$ antisite defects. Therefore, LFP/C materials with high tap densities and superior electrochemical characteristics can be used in electrodes for large-scale applications requiring both high capacity and excellent rate performance.

Acknowledgements

This work was supported by the Advanced Technology Center (ATC) Program (No.10035919) funded by the Ministry of Trade, industry & Energy (MI, Korea) ; World Premier Materials grant funded by the Korea government Ministry of Trade, Industry and Energy ; the Human Resources Development program (20124010203320) of the Korea Institute of Energy Technology Evaluation and Planning (KETEP) grant funded by the Korea government Ministry of Trade, Industry and Energy.

Notes and references

[a] *Energy Efficient Materials Team, Energy & Environmental Division, Korea Institute of Ceramic Engineering & Technology, 233-5 Gasan-dong, Guemcheon-gu, Seoul 153-801, Republic of Korea. Fax: +82-2-3282-2475; Tel: +82-2-3282-2463: E-mail: rkc@kicet.re.kr.*

[b] *Department of Materials Science & Engineering, Yonsei University, 50 Yonsei-ro, Seodaemun-gu, Seoul 120-749, Republic of Korea.*

[c] *Department of Materials Science and Engineering, Seoul National University, 599 Gwanak-ro, Gwanak-gu, Seoul 151-741, Republic of Korea. Fax: +82-2-885-9671; Tel: +82-2-880-7165: E-mail: matlgen1@snu.ac.kr.*

[d] *Department of Energy Engineering, Dankook University, Cheonan 330-714, Republic of Korea.*

[e] *Center for Nanoparticle Research, Institute for Basic Science (IBS), Seoul National University, 1 Gwanak-ro, Gwanak-gu, Seoul 151-742, Republic of Korea.*

† Electronic Supplementary Information (ESI) available: FE-SEM images of the precursors prepared for different times; nitrogen adsorption-desorption; Rietveld refinements of the XRD patterns. See DOI: 10.1039/b000000x/

1 A. S. Andersson, J. O. Thomas, B. Kalska and L. Häggström, *Electrochem. Solid-State Lett.*, 2000, **3**, 66.

2 J. Wang and X. Sun, *Energy Environ. Sci.*, 2012, **5**, 5163.

3 X. Qin, J. Wang, J. Xie, F. Li, L. Wen and X. Wang, *Phys. Chem. Chem. Phys.*, 2012, **14**, 2669.

4 R. Malik, D. Burch, M. Bazant and G. Ceder, *Nano Lett.,* 2010, **10**, 4123.

5 P. P. Prosini, M. Carewska, S. Scaccia, P. Wisniewski and M. Pasquali, *Electrochim. Acta.,* 2003, **48**, 4205.

6 A.D. Spong, G. Vitins and J.R. Owen, *J. Electrochem. Soc.*, 2005, **152**, A2376.

7 Y. Wang, J. Wang, J. Yang and Y. Nuli, *Adv. Funct. Mater.,* 2006, **16**, 2135

8 H. Shu, X. Wang, Q. Wu, B. Ju, L. Liu, X. Yang, Y. Wang, Y. Bai and S. Yang, *J. Electrochem. Soc.,* 2011, **158**, A1448.

9 S. W. Oh, S.-T. Myung, S.-M. Oh, K. H. Oh, K. Amine, B. Scrosati and Y.-K. Sun, *Adv. Mater.,* 2010, **22**, 4842.

10 C. Sun, S. Rajasekhara, J. B. Goodenough and F. J. Zhou, *J. Am. Chem. Soc.,* 2011, **133**, 2132.

11 B. Kang and G. Ceder, *Nature,* 2009, **458**, 190.

12 J. Qian, M. Zhou, Y. Cao, X. Ai and H. J. Yang, *J. Phys. Chem. C,* 2010, **114**, 3477.

13 M.-Y. Cho, K.-B. Kim, J.-W. Lee, H. Kim, H. Kim, K. Kang and K. C. Roh, *RSC Advances,* 2013, **3**, 3421.

14 G. Meligrana, C. Gerbaldi, A. Tuel, S. Bodoardo and N. J. Penazzi, *J. Power Sources,* 2006, **160**, 516.

15 W. Li, Y.-C, Han, J.-L. Zhang and B.-G. Wang, *Colloid J.,* 2005, **67**, 186.

16 Q. Liu, L.-N. Jin and W.-Y. Sun, *Chem. Commun.,* 2012, **48**, 8814.

17 E. V. Shevchenko, D. V. Talapin, H. Schnablegger, A. Kornowski, Ö. Festin, P. Svedlindh, M. Haase and H. J. Weller, *J. Am. Chem. Soc.,* 2003, **125**, 9090.

18 A. C. Pierre, *Introduction to Sol-Gel Processing*, Kluwer, Boston, 1998, p. 92.

19 H. Yang, X. -L. Wu, M. -H. Cao and Y. -G. Guo, *J. Phys. Chem. C,* 2009, **113**, 3351.

20 J. Chen, S. Wang and M. S. Whittingham, *J. Power Sources,* 2007, **174**, 442.

21 F. Brochu, A. Guerfi, J. Trottier, M. Kopeć, A. Mauger, H. Groult, C. M. Julien and K. J. Zaghib, *J. Power Sources,* 2012, **214**, 1.

22 R. Dedryvère, M. Maccario, L. Croguennec, F. Le Cras, C. Delmas and D. Gonbeau, *Chem. Mater.,* 2008, **20**, 7164.

Size-selective Synthesis of Mesoporous $LiFePO_4$/C Microspheres based on Nucleation and Growth Rate Control of Primary Particles

Min-Young Cho[a,b], Haegyeom Kim[c], Hyungsub Kim[c], Young Su Lim[a], Kwang-Bum Kim[b], Jae-Won Lee[d], Kisuk Kang[c,e]*, and Kwang Chul Roh[a,]*

Table of contents entry

$LiFePO_4$/C microparticles with various sizes (3–7 μm) and tap densities (1.3–1.5 g cm^{-3}) are successfully synthesized by adjusting the nucleation and growth rate using cetyltrimethylammonium bromide (CTAB) as cationic surfactant. The synthesized $LiFePO_4$/C particles exhibit excellent gravimetric and volumetric rate capabilities by a low antisite defect and mesoporous structure.